Research Square

Preprints are preliminary reports that have not undergone peer review.
They should not be considered conclusive, used to inform clinical practice,
or referenced by the media as validated information.

Halide Perovskite Trilayer Metasurfaces for Ultrabright and Wide-Gamut Structural Color

Rukon Uddin

rukon2k13@gmail.com

Noakhali Science and Technology University

Research Article

Keywords: halide perovskite, metasurface, structural color, Mie resonance, truncated cone, FDTD, $CsPbI_3$, $MAPbCl_3$, CIE 1931, color gamut

Posted Date: September 12th, 2026

DOI: https://doi.org/10.21203/rs.3.rs-10999548/v1

License: This work is licensed under a Creative Commons Attribution 4.0 International License.
Read Full License

Additional Declarations: The authors declare no competing interests.

Halide Perovskite Trilayer Metasurfaces for Ultrabright and Wide-Gamut Structural Color

Rukon Uddin

Abstract

We present an all-perovskite, gradient-index trilayer metasurface for reflective structural color based on a truncated-cone meta-atom comprising a black-phase α-$CsPbI_3$ core between two $MAPbCl_3$ cladding layers. The design translates the multilayer gradient-index concept previously demonstrated with GaP/TiO_2 into a chemically related halide-perovskite platform. Finite-difference time-domain (FDTD) simulations show that, with the three-layer heights fixed at 90/100/80 nm, the palette can be generated primarily by scaling the lateral radii and lattice period. Seven representative colors are obtained with peak reflectance near unity in the reported simulations and resonance peaks spanning 470–630 nm. The calculated linewidth decreases from 63 nm for the shortest-wavelength design to approximately 19 nm for the red design. Near-field maps of the red structure are consistent with a magnetic-dipole-dominated Mie resonance localized predominantly within the high-index $CsPbI_3$ core. The circular in-plane symmetry gives polarization-insensitive behavior at normal incidence, while the angular maps indicate that the resonance remains identifiable to oblique incidence approaching approximately 40–50°. The corresponding CIE 1931 coordinates demonstrate a broad chromaticity range, with the violet, blue, and cyan designs extending beyond the sRGB gamut while the full set lies within the reported Adobe RGB and Rec. 2020 reference triangles. The results establish a simulation-level proof of concept for an all-perovskite structural-color architecture. Practical implementation will require careful control of the optical constants, phase stability of α-$CsPbI_3$, film quality, and nanofabrication compatibility.

Keywords: halide perovskite; metasurface; structural color; Mie resonance; truncated cone; FDTD; $CsPbI_3$; $MAPbCl_3$; CIE 1931; color gamut

1. Introduction

Structural color provides a route to coloration and spectral filtering through wavelength-selective scattering from subwavelength or near-subwavelength structures rather than

molecular absorption, which is the mechanism underlying conventional organic dyes and pigments and their associated stability limitations [1]. Plasmonic nanostructures offer high spatial resolution, but Ohmic dissipation can substantially reduce the useful reflected intensity [2], [3]. All-dielectric metasurfaces avoid metal loss and can support electric- and magnetic-type Mie resonances with comparatively low dissipative loss, making high-index dielectric resonators such as silicon and TiO_2 important platforms for structural color [4], [5]. These materials nevertheless impose design constraints. Silicon exhibits appreciable absorption toward the blue/violet region, while TiO_2, despite its low visible absorption, generally provides a lower refractive-index contrast than high-index semiconductors and can therefore require larger or more strongly optimized resonators for narrow, high-contrast resonances [5]–[7].

A recent multilayer truncated-cone architecture addressed this trade-off by combining GaP and TiO_2 in a vertically structured, tapered meta-atom. The reported design used the material contrast and tapered geometry to reshape the modal response and achieved reflectivity as high as 93% together with a color gamut extending beyond the Rec. 2020 reference triangle [8]. The broader design lesson is that a multilayer resonator can distribute electromagnetic confinement and radiation among compositionally distinct regions, allowing material dispersion and geometry to work together. The present work asks whether that design principle can be transferred to a chemically related halide-perovskite system while retaining a compact, common vertical architecture.

Halide perovskites are attractive for this purpose because they combine strong optical response with composition-dependent electronic and optical properties. The $CsPbX_3$ family exhibits composition-dependent band gaps and visible optical response, and halide exchange provides an additional route for modifying optical properties [11]–[14]. Perovskite nanostructures have also been investigated as active and resonant elements in meta-optics, including structural-color and dynamically tunable platforms [15], [16]. These characteristics make perovskites more than a passive replacement for conventional dielectrics: the material composition itself can become an optical-design variable. In the present manuscript, however, the seven-color demonstration is produced by geometric scaling while the layer compositions and vertical dimensions are kept fixed; composition tuning is discussed as a future extension rather than treated as an additional simulation variable.

The proposed architecture therefore combines a high-index resonant core with wider-bandgap perovskite cladding layers. The use of $CsPbI_3$ for the central region is motivated by its high

refractive index and narrow band gap, whereas $MAPbCl_3$ is selected as the wide-bandgap cladding material because of its comparatively transparent visible spectral window and demonstrated thin-film/single-crystal quality [17]–[20]. Keeping the three layers within the halide-perovskite family offers a chemically unified alternative to a GaP/TiO_2 stack and may simplify the conceptual fabrication sequence. The design should nevertheless be understood as a simulated architecture rather than as an experimentally demonstrated process.

A central practical limitation is the phase stability of black α-$CsPbI_3$. At ambient conditions, the desired black perovskite phase is metastable and can transform toward a non-perovskite yellow phase unless stabilized [21]. This limitation is particularly important here because the optical function of the resonator depends on the refractive index of the intended phase. Consequently, any experimental realization would require an appropriate stabilization strategy, such as compositional engineering, strain/structural stabilization, or encapsulation, and the optical constants of the stabilized material would need to be verified experimentally before device fabrication.

Building on this material pairing, we designed a trilayer truncated-cone meta-atom and used geometric scaling to generate a seven-color palette. The three vertical layer heights were fixed at 90, 100, and 80 nm, while the radii and lattice period were varied between color designs. This produces a common vertical architecture and shifts the resonant wavelength primarily through lateral scaling. The resulting structures span violet through red in the simulated reflectance spectra. The contribution of the present work is therefore a simulation-based design framework that combines gradient-index geometry with a chemically unified halide-perovskite material system, rather than a claim of experimentally realized all-perovskite structural color. This places the present design at the intersection of two lines of work that have so far stayed largely separate: the geometry-driven, gradient-index metasurface strategy demonstrated with GaP and TiO_2 [8], and the composition-driven tunability that is characteristic of halide perovskites [11]–[16].

2. Modeling and Simulation

All optical simulations were carried out using the finite-difference time-domain (FDTD) method in Lumerical FDTD Solutions. The unit cell contains one trilayer truncated-cone meta-atom on a fused-silica substrate: a bottom $MAPbCl_3$ frustum, a central $CsPbI_3$ frustum, and a top $MAPbCl_3$ frustum sharing a common axis, as shown in Figure 1. FDTD solves Maxwell's

equations directly in the time domain, allowing broadband spectral response to be evaluated from a single excitation. The formulation used here follows the standard Maxwell curl equations and Yee-grid time stepping originally described by Yee [22], following the implementation conventions summarized by Taflove and Hagness [23].

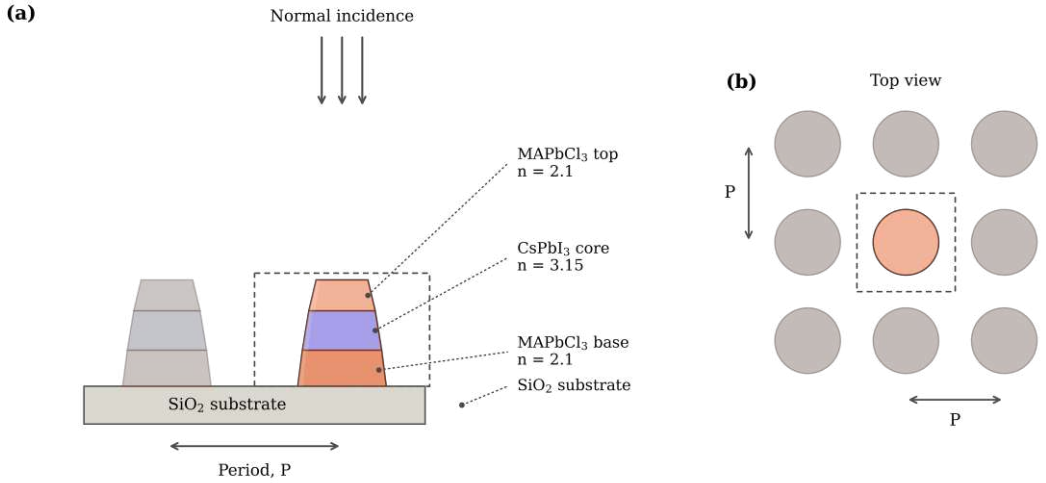


Figure 1. (a) Side view of the periodic trilayer truncated cone array, with the highlighted unit cell showing the MAPbCl3 top and base frustums, the CsPbI3 core frustum, the SiO2 substrate, the lattice period P, and the normal incidence illumination used in all simulations. (b) Top view of the square lattice showing the period P along both in-plane directions.

$$\frac{\partial \mathbf{H}}{t} = -\frac{1}{\mu} \nabla \times \mathbf{E} \tag{1}$$

$$\frac{\partial \mathbf{E}}{t} = \frac{1}{\varepsilon} \nabla \times \mathbf{H} - \frac{\sigma}{\varepsilon} \mathbf{E} \tag{2}$$

where E and H are the electric and magnetic field vectors, ε and μ are the local permittivity and permeability, and σ is the electric conductivity. The method discretizes space and time on a staggered Yee grid, updating E and H in an alternating leapfrog sequence so that each new value depends only on already computed values of the other field, without requiring any matrix inversion. A representative update, taking the Hx component as an example, has the form

$$\mathbf{H}_x{}^{n+\frac{1}{2}}\left(i, j+\frac{1}{2}, k+\frac{1}{2}\right) = \mathbf{H}_x{}^{n-\frac{1}{2}}\left(i, j+\frac{1}{2}, k+\frac{1}{2}\right) + \frac{\Delta t}{\mu \Delta y}\left[\mathbf{E}_y{}^{n}(i, j, k+1) - \mathbf{E}_y{}^{n}(i, j, k)\right] - \frac{\Delta t}{\mu \Delta z}\left[\mathbf{E}_z{}^{n}\left(i, j+1, k+\frac{1}{2}\right) - \mathbf{E}_z{}^{n}\left(i, j, k+\frac{1}{2}\right)\right] \tag{3}$$

The spatial step and the time step are linked through the Courant Friedrichs Lewy stability condition

$$\Delta t \leq \frac{1}{c\sqrt{\frac{1}{\Delta x^2}+\frac{1}{\Delta y^2}+\frac{1}{\Delta z^2}}} \tag{4}$$

A broadband Bloch-periodic plane-wave source was used for normal-incidence illumination over 400–800 nm, with periodic boundary conditions in the two in-plane directions and a perfectly matched layer in the vertical direction. A local mesh override was applied around the meta-atom, and the red design was rerun with a finer mesh as a convergence check before the same numerical settings were applied to the remaining designs. Reflection and transmission were recorded using frequency-domain power monitors, and the simulated spectra were converted to CIE 1931 chromaticity coordinates under the stated D65 illuminant and 2° observer. For the six additional colors, the radii and lattice period were scaled toward the desired spectral region while the three layer heights were retained. Each final geometry was then evaluated with its own broadband simulation.

A truncated-cone geometry was selected instead of a straight cylinder to introduce a controlled vertical geometry/index gradient and to modify the modal overlap within the resonator. The taper also provides two lateral radii per layer, increasing geometric degrees of freedom without changing the total etch depth. Figure 2 compares the two geometries directly for the cyan design, with the cylinder built at the same period and height and using the cone's base radius as its fixed radius. The cylinder shows a broad, double lobed reflectance band spanning roughly 480 to 600 nm, with a shallow dip near 520 nm and a secondary low amplitude feature near 420 to 460 nm. The truncated cone collapses this into a single, narrower peak near 515 to 520 nm and removes the short wavelength secondary feature almost entirely. This is the same qualitative outcome reported when shape modification is used to selectively damp higher order Mie resonances while preserving a fundamental mode in dielectric lattice resonators [25], and it is consistent with tapering suppressing a competing electric-dipole-like contribution rather than simply narrowing the fundamental linewidth by chance. In this study, the near-field maps in Figure 6 independently identify the dominant resonance of the truncated-cone design as magnetic-dipole-like. Together, the cylinder comparison and the near-field maps support the taper as the mechanism suppressing the competing mode, though the manuscript stops short of a formal multipole decomposition; quantitatively separating electric, magnetic, and higher-order Cartesian multipole contributions would be a useful, direct extension of this comparison.

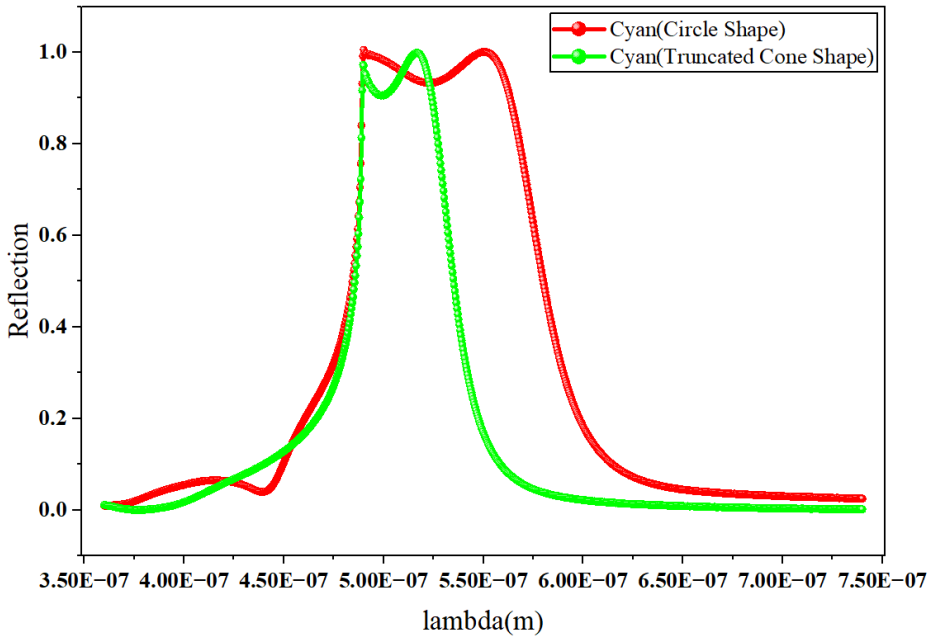


Figure 2. Simulated reflectance for the cyan design using a straight cylinder versus the truncated-cone geometry used throughout this work, with period, height, and base radius held equal between the two cases.

2.1 Design rationale and modeling scope

The design separates the optical roles of the three layers. The central α-$CsPbI_3$ region provides the high-index volume in which the principal Mie resonance is concentrated, while the $MAPbCl_3$ layers form the surrounding optical environment and complete the vertical gradient. The color palette is generated by changing lateral dimensions rather than by changing the layer materials or their heights. This separation distinguishes the principal structural tuning variables (radius and period) from the selected material system and keeps the seven designs within a common vertical architecture.

Table 1. Design rationale and practical scope of the present simulation study.

Element	Primary role	What the present study demonstrates	Practical qualification
α-$CsPbI_3$ core	High-index resonant volume	Near-field response consistent with a magnetic-dipole-like Mie mode	Black α-phase is metastable and requires stabilization

$MAPbCl_3$ cladding	Wide-bandgap surrounding optical environment	Common top and bottom layers retained across all designs	Optical loss and complex refractive index should be experimentally verified
Frustum taper	Vertical geometry/index gradient and additional radius control	Radius and height sweeps support geometric tuning	No formal multipole decomposition is claimed
Lattice period Λ	Array spacing and spectral placement	Varied with lateral dimensions to generate the palette	Should remain compatible with the intended localized-resonance regime
Fixed heights 90/100/80 nm	Common vertical architecture	All seven designs use total height H = 270 nm	Common design target, not experimental fabrication validation
CIE 1931 analysis	Quantification of simulated color	Chromaticity coordinates and excitation purities are reported	Final appearance also depends on illumination, viewing geometry, and fabrication

2.2 Numerical interpretation and limits

The reported results are numerical predictions for the specified material and geometric model. Peak reflectance is therefore reported as approximately unity rather than as physically greater than 100%, because the original monitor output contained small normalization overshoots. The optical constants listed with the designs are model inputs; near an absorption edge, quantitative predictions can be sensitive to the wavelength dependence of both the real and imaginary parts

of the refractive index. The present study consequently emphasizes the feasibility and design logic of the architecture rather than claiming experimental performance or a material-independent scaling law.

3. Results and Discussion

The results are organized around four questions: (i) whether the resonant color response is robust to polarization and incidence angle, (ii) how the resonance responds to the principal geometric parameters, (iii) what electromagnetic mode dominates the representative red design, and (iv) whether the same fixed-height architecture can generate a broad visible palette. The final designs are summarized in Table 2 and their chromaticity is compared with standard display gamuts in Figure 7.

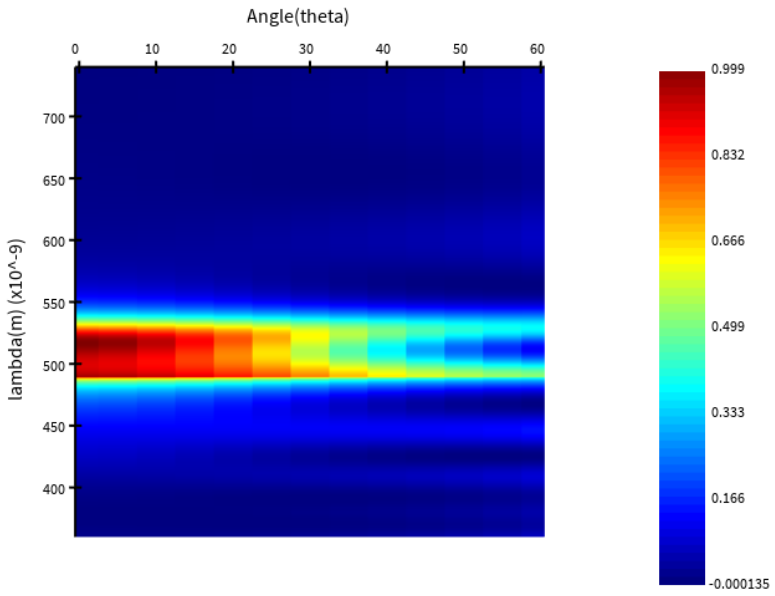


Figure 3a. Wavelength- and angle-resolved reflectance under 90° (S-polarized) illumination for a representative mid-palette (cyan) design, for angles of incidence 0–60°.

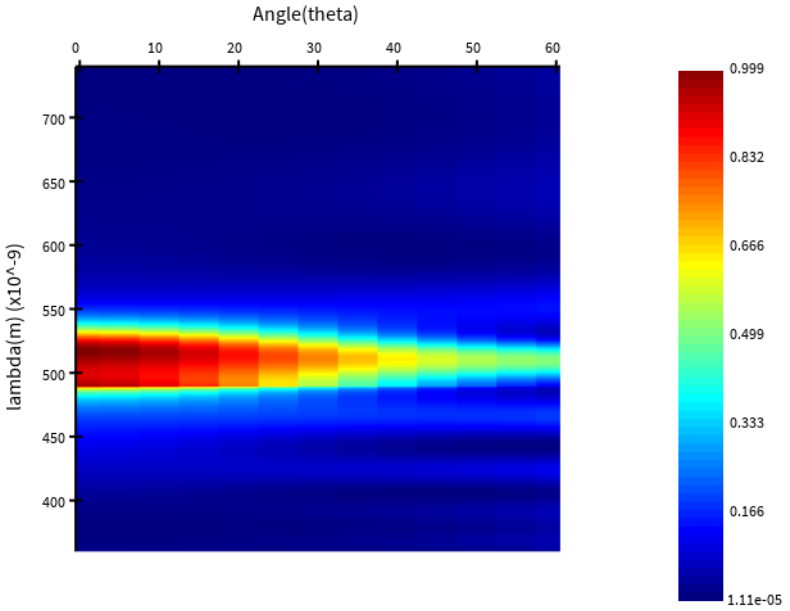


Figure 3b. The same map under 0° (P-polarized) illumination.

The two polarization maps are essentially indistinguishable within the numerical resolution of the simulations. This behavior is consistent with the circular in-plane symmetry of the meta-atom and is expected for normal incidence; at oblique incidence, the two polarization channels can in general differ, so the reported agreement across the angular sweep is an important numerical observation rather than a consequence that should be assumed a priori. The resonance remains clearly identifiable through approximately 30° and its spectral feature persists to larger angles, with the reported peak response remaining above half maximum to approximately 50–60°. The relatively moderate angular dispersion is consistent with a localized resonant response rather than a purely grating-mediated color mechanism, although the practical viewing-angle performance should ultimately be assessed using color-coordinate shifts rather than resonance visibility alone.

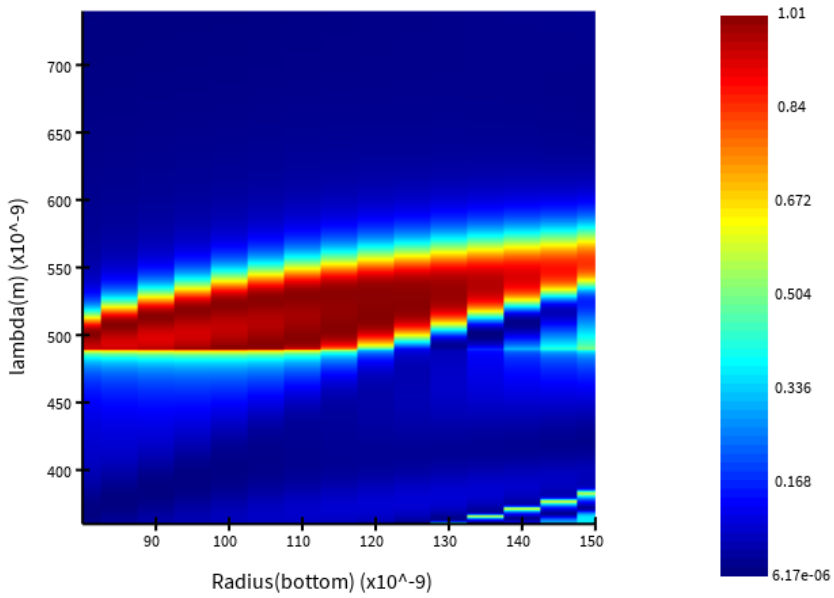


Figure 4. Reflectance as a function of wavelength and bottom-frustum radius, with all other parameters fixed at the red design's values.

Figure 4 shows a monotonic dependence of the resonance wavelength on the bottom-frustum radius over the investigated range. Increasing the radius from approximately 80 to 150 nm produces a red shift of roughly 35–40 nm while maintaining peak reflectance above 0.9 over most of the sweep. This smooth dependence provides the basis for the palette-scaling strategy: lateral dimensions can be increased systematically to move the resonance toward longer wavelengths while the vertical layer thicknesses remain unchanged. The result is a practical geometric design rule within the parameter range investigated, rather than a universal linear scaling law for arbitrary perovskite geometries.

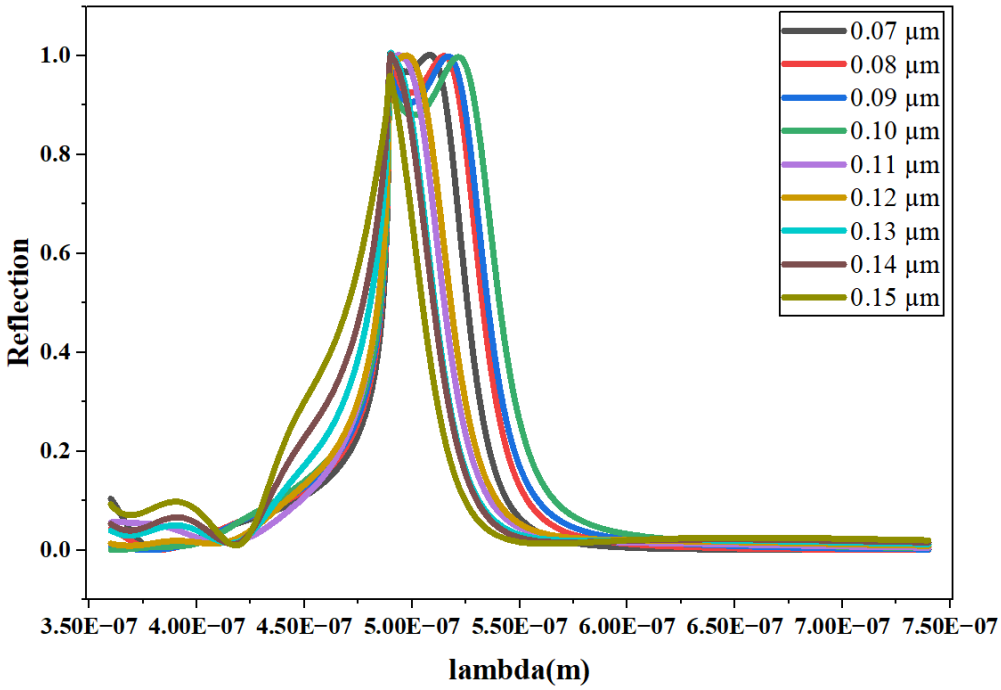


Figure 5. Reflectance spectra for top-frustum heights from 70 to 150 nm, all other parameters held at the red design's values.

The dependence on top-frustum height is non-monotonic rather than a simple red shift. Increasing height from 70 to approximately 100 nm produces a modest red shift of roughly 10–15 nm with a comparatively clean single-peak lineshape. Increasing height further, from 100 to 150 nm, reverses this trend: the resonance blue-shifts by roughly 35–40 nm relative to the 100 nm case, and the shortest and tallest structures in the sweep both develop a shouldered or two-lobed spectral response, consistent with additional modal content entering the spectral region as the structure becomes electrically larger or smaller relative to the resonance condition. The cleanest, most red-shifted single-peak response in the investigated sweep occurs near 80–90 nm, motivating the selected 80 nm bottom cladding thickness. The central and top layer heights were likewise fixed at 90 and 100 nm, respectively, and subsequently retained across the color palette.

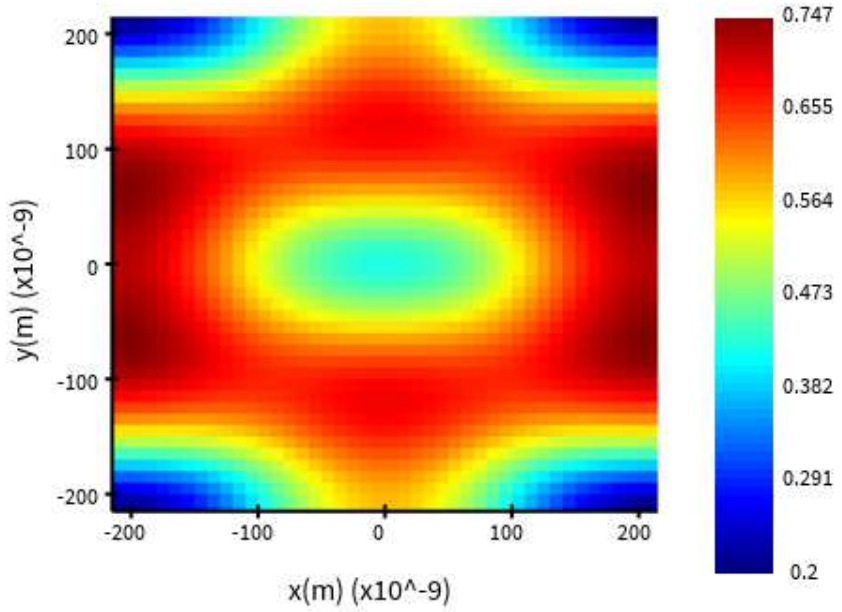


Figure 6a. In-plane electric-field intensity $|E|^2$ of the red design at resonance, taken through the core mid-plane.

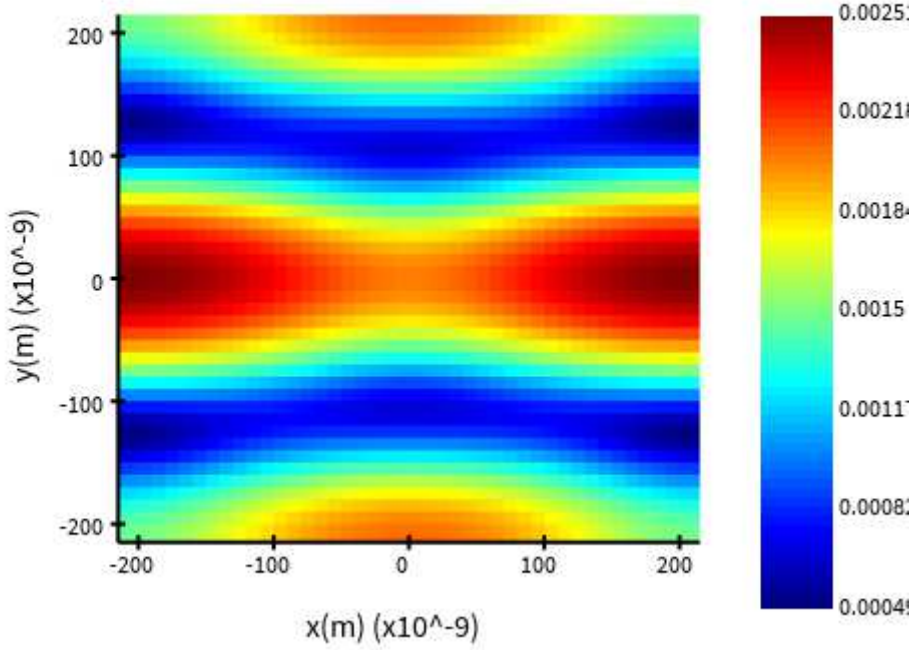


Figure 6b. In-plane magnetic-field intensity $|H|^2$ at the same cross-section.

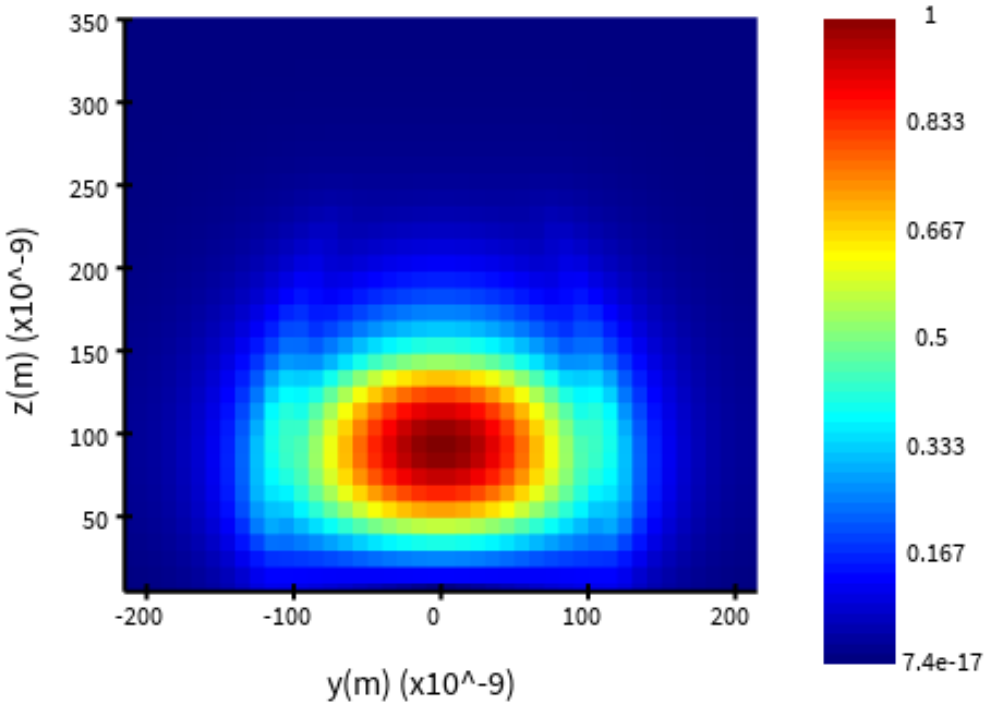


Figure 6c. Vertical (y–z) cross-section of the field intensity through the meta-atom.

The near-field distributions in Figure 6 are consistent with a magnetic-dipole-like Mie resonance. The in-plane electric field forms a circulating pattern around the resonator center, while the magnetic field exhibits strong concentration within the resonant region. The vertical cross-section further indicates that the strongest field confinement is associated with the lower portion of the stack and the $MAPbCl_3$/$CsPbI_3$ interface, supporting the interpretation that the high-index $CsPbI_3$ region is the principal resonant volume while the $MAPbCl_3$ layers provide the surrounding index environment. Because these maps do not constitute a formal multipole decomposition, the mode assignment is intentionally described as magnetic-dipole-like rather than as exclusive proof that all competing multipoles are negligible. In particular, the circulating in-plane electric field is also the signature associated with toroidal dipole excitation in related dielectric and metamaterial resonators [9], [10], so a toroidal contribution cannot be excluded from the present maps alone and would need to be checked explicitly in a full multipole decomposition.

Table 2. Structural parameters of the all-perovskite trilayer frustum meta-atoms ($MAPbCl_3$ cladding / α-$CsPbI_3$ core) and their simulated optical response for the seven-color palette.

R_bottom and R_top denote the wide (substrate-side) and narrow (top) radii of each truncated-cone segment; segment heights are fixed across the palette, and the color palette is generated entirely by scaling radius and lattice period.

Structural design parameters (all-perovskite trilayer frustum meta-atom)								
Layer	**Parameter**	Violet (470 nm)	Blue (495 nm)	Cyan (516 nm)	Green (549 nm)	Yellow (579 nm)	Orange (602 nm)	Red (630 nm)
Bottom cladding $MAPbCl_3$ (nominal n = 2.10)	R_bottom (nm)	89	95	101	109	118	124	130
	R_top (nm)	82	88	93	101	109	114	120
	Height (nm)	90	90	90	90	90	90	90
Core $CsPbI_3$ (nominal n = 3.15)	R_bottom (nm)	82	88	93	101	109	114	120
	R_top (nm)	68	73	78	84	91	95	100
	Height (nm)	100	100	100	100	100	100	100
Top cladding $MAPbCl_3$ (nominal n = 2.10)	R_bottom (nm)	68	73	78	84	91	95	100
	R_top (nm)	48	51	54	59	63	67	70
	Height (nm)	80	80	80	80	80	80	80

Period, Λ (nm)	**293**	**314**	**334**	**362**	**389**	**410**	**430**
Total meta-atom height, H (nm)	**270**	**270**	**270**	**270**	**270**	**270**	**270**
Simulated optical response (CIE 1931 2° observer, D65 illuminant)							
Peak reflectance wavelength, λ_peak (nm)	470	495	516	549	579	602	630
Peak reflectance, R_peak (%)	≈100	≈100	≈99.9	≈99.8	≈100	≈100	≈100
FWHM (nm)	63	58	49	41	33.4	23	19.3
CIE dominant wavelength, λ_d (nm)	468	483	503	545	576	590	604
Excitation purity, p_e (%)	91.5	79.7	58.4	70.0	87.2	84.9	58.3
CIE chromaticity (x, y)	0.1457, 0.0717	0.1240, 0.2077	0.1328, 0.4865	0.2820, 0.6040	0.4637, 0.4895	0.5379, 0.4076	0.5061, 0.3442

The asterisked values in the original FDTD monitor output exceeded unity by a small numerical normalization amount. Because passive reflectance cannot physically exceed 100%, the main table reports these cases as approximately 100% rather than presenting values above unity as physical reflectance. The raw monitor overshoot is retained only as a numerical note and is not interpreted as optical gain. Table 3 lists these raw per-color monitor values directly for traceability against the underlying simulation output. Re-extraction of the peak positions and full widths at half maximum directly from the simulated spectra additionally identified a 1 nm correction to the orange design's peak wavelength, from 601 to 602 nm, which is reflected throughout this manuscript.

Table 3. Raw FDTD monitor peak values by color, extracted directly from the simulated reflectance spectra. Values slightly above 100% arise from numerical normalization in the

monitor output and are not interpreted as physical reflectance above unity; the main text and Table 2 report these cases as approximately 100%.

Color	Violet	Blue	Cyan	Green	Yellow	Orange	Red
Raw FDTD peak (%)	100.044	100.050	99.869	99.781	99.995	100.909	101.346

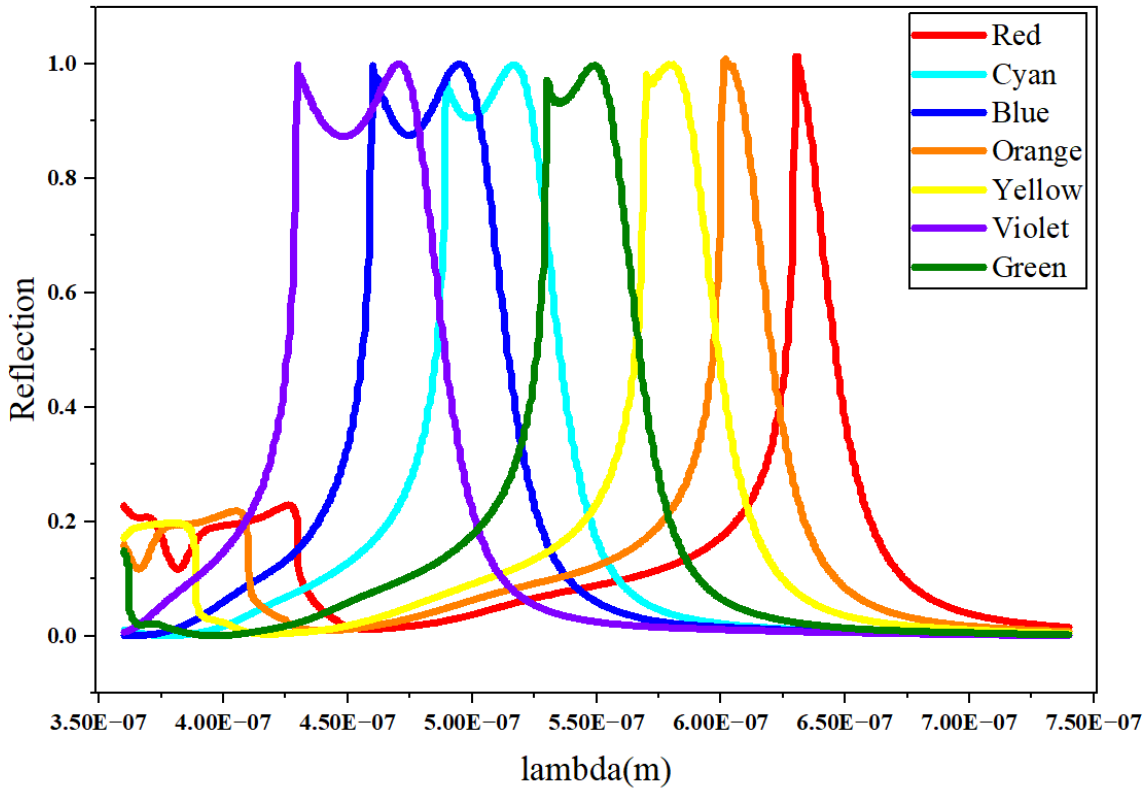


Figure 7. Simulated reflectance spectra of the seven finalized designs, plotted together on a common wavelength axis.

Figure 7 and Table 2 summarize the finalized palette. The calculated peak reflectance is approximately unity for all seven designs, with the raw monitor output showing small normalization excursions above 100% for the two longest-wavelength cases; these excursions are numerical and are not interpreted as gain. The resonance linewidth decreases from 63 nm for violet to approximately 19 nm for red. This trend should be interpreted within the optical-constant model used in the simulations and with particular caution near the $MAPbCl_3$ absorption edge, where changes in the complex refractive index can affect both resonance

position and linewidth. The excitation-purity values likewise vary across the palette, reflecting the location of each calculated chromaticity coordinate relative to the spectral locus and the shape of the broadband reflectance spectrum.

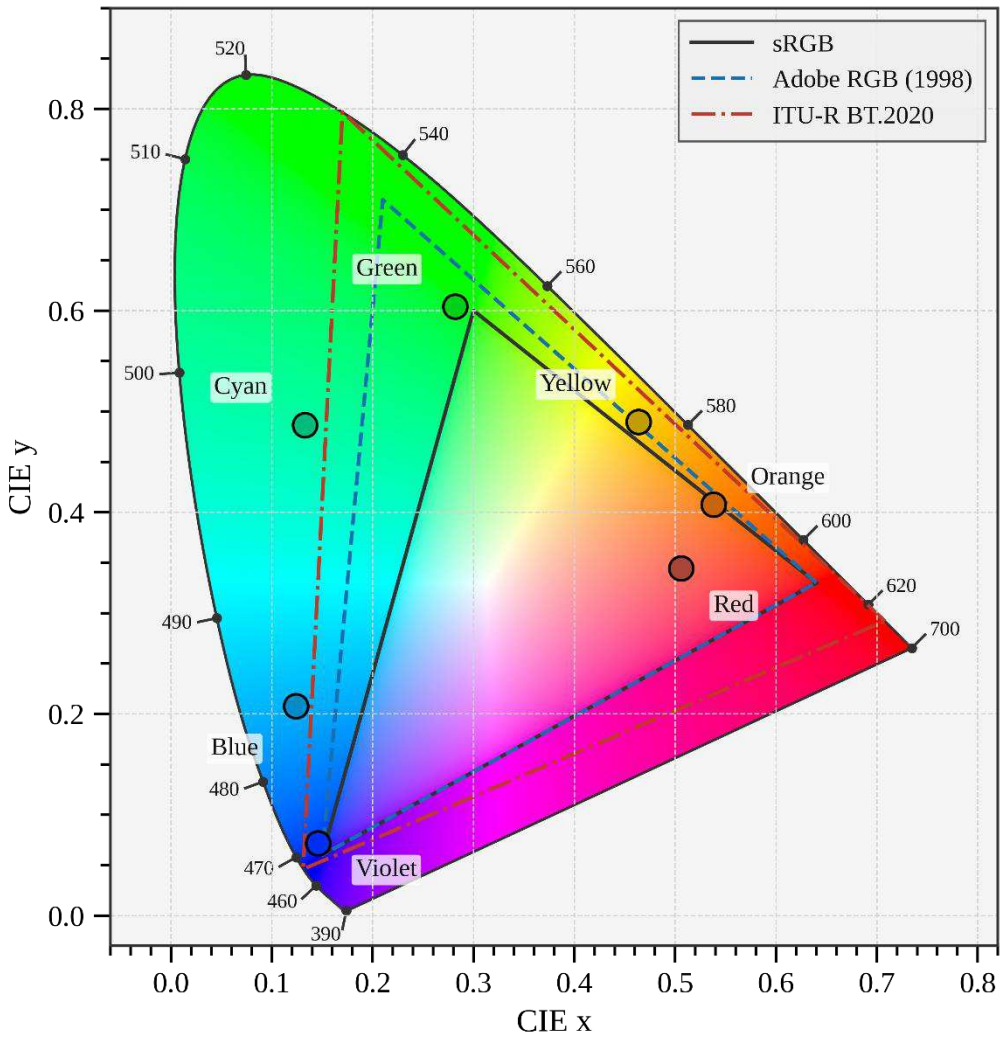


Figure 8. CIE 1931 [24] chromaticity coordinates of the seven designs (filled circles, colored to their approximate sRGB rendering) plotted against the sRGB, Adobe RGB (1998), and Rec. 2020 gamut triangles under the D65 illuminant.

The seven calculated chromaticity coordinates occupy a broad region of the CIE 1931 diagram. The violet, blue, and cyan points extend beyond the sRGB triangle, while the complete set of points lies within the Adobe RGB and Rec. 2020 reference triangles shown in Figure 8. This indicates access to saturated colors that are not fully represented by the smaller sRGB gamut. The CIE analysis should be interpreted as a colorimetric assessment of the simulated spectra rather than as a direct prediction of perceived color under every viewing condition; illumination spectrum, surface scattering, viewing geometry, and fabrication-induced spectral broadening

can all alter the final appearance. Nevertheless, the calculated coordinates demonstrate that the proposed architecture has sufficient spectral selectivity to cover a broad visible color space.

Table 4. Key quantitative outcomes of the reported design study.

Metric	Reported result	Interpretation
Color span	470–630 nm peak reflectance	Seven representative colors from violet to red
Peak reflectance	≈100% for all seven designs	Near-unity simulated reflection; raw monitor overshoots are numerical
FWHM	63–20 nm	Progressive narrowing from violet toward red
Angular response	Resonance identifiable to ~40–50°; above half maximum to ~50–60° in the representative map	Indicates useful angular tolerance in the simulated structure
Polarization	S and P maps essentially indistinguishable in the reported sweep	Consistent with rotational symmetry and the calculated response
Palette geometry	90/100/80 nm layer heights; lateral radii and period varied	Common vertical architecture across the seven designs
Color gamut	Violet/blue/cyan extend beyond sRGB; all seven points within the reported Adobe RGB and Rec. 2020 triangles	Broad simulated chromaticity coverage

The present work is intentionally limited to the simulation results already described and does not introduce additional numerical datasets. Four considerations are especially important for

translation toward experiment. First, the optical response depends directly on the complex refractive indices assigned to α-$CsPbI_3$ and $MAPbCl_3$; measured wavelength-dependent optical constants for the actual deposited films should therefore be used in an experimental design cycle. Second, the phase stability of α-$CsPbI_3$ is a materials constraint rather than a minor fabrication detail. Third, nanoscale dimensional errors, sidewall-angle variation, surface roughness, and interfacial defects can broaden or shift resonances relative to the ideal geometry. Finally, the calculated CIE coordinates describe ideal simulated spectra and do not by themselves establish color stability under different illumination and viewing conditions. These considerations define the most direct experimental validation path without changing the central architecture proposed here.

Comparison with previously reported works

Table 5 places the present simulation results next to previously reported structural color metasurface platforms built from single or dual dielectric materials, including the GaP/TiO2 trilayer that motivated the present design. The comparison is intended to show where the simulated perovskite trilayer sits relative to established, experimentally verified designs, not to claim equivalence between simulated and measured performance.

Table 5. Comparison of the present simulation results with previously reported structural color metasurface platforms. The Si cylindrical metasurface gamut is as reported directly in [5]; the TiO2 square metasurface reflectance figures are as reported by Miah et al. [8], who compared against the original source [7]. The reflectance range for the multipolar-modulated Si metasurface is as reported directly in [27].

Platform	Material system	Fabrication status	Peak reflectance	Reported gamut	Ref.
This work	MAPbCl3 / CsPbI3 / MAPbCl3 trilayer frustum	Simulation (FDTD) only	≈100% (simulated)	Violet, blue, cyan beyond sRGB; full set within Adobe	—

				RGB and Rec. 2020	
GaP/TiO2 trilayer frustum	GaP core, TiO2 cladding	Fabricated and measured	70–93% (avg. 83%)	222.1% sRGB, 164.5% Adobe RGB, 117.4% Rec. 2020	[8]
Si cylindrical metasurface	Silicon (DMSO environment)	Fabricated and measured	15–74%	181.8% sRGB, 135.6% Adobe RGB, 97.2% Rec. 2020	[5]
TiO2 square metasurface	TiO2	Fabricated and measured	~60% (blue-violet), <70% overall	Not reported	[7]
MAPbX3 perovskite grating	MAPbBr3 / MAPbX3 (mixed halide)	Fabricated and measured	Narrow, intense peaks (% not reported)	Not reported	[26]
Multipolar-modulated Si metasurface	Silicon (multi-dielectric stack)	Fabricated and measured	70–90%	Not reported	[27]

The simulated reflectance of the perovskite trilayer is comparable to, or higher than, the experimentally measured values reported for the silicon and TiO2 platforms, and falls within the range demonstrated experimentally for the GaP/TiO2 trilayer that motivated the present design. This agreement should be read carefully. The GaP/TiO2, silicon, and TiO2 platforms in Table 5 are backed by fabrication and optical measurement, while the perovskite trilayer

reported here has only been evaluated numerically. The comparison therefore indicates that the simulated design is not obviously unrealistic relative to established structural color platforms, rather than establishing that it will reproduce these numbers once fabricated. The multipolar-modulated silicon platform in Table 5 is a particularly close conceptual comparison: it also uses index-matched multilayer stacking to suppress competing modes and improve color purity, the same design logic applied here through the truncated-cone geometry compared directly in Figure 2.

4. Limitations and experimental outlook

4.1 Tolerance of radius

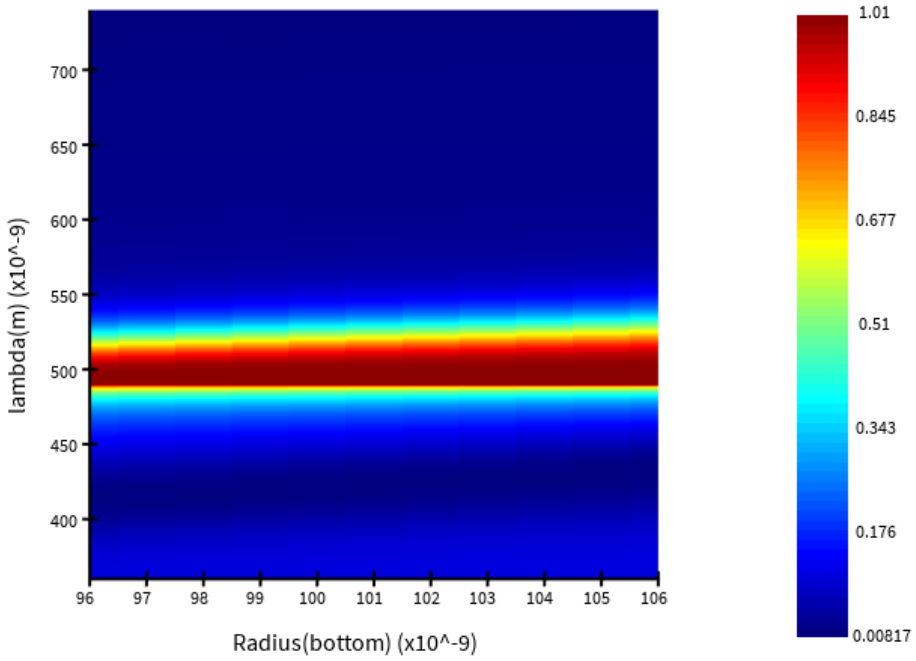


Figure 9. Fine radius tolerance sweep. Wavelength resolved reflectance as a function of bottom radius over a 96 to 106 nm window, with all other parameters held at their nominal design values.

Figure 9 shows a fine radius sweep across a 10 nm window centered on a representative design point. Within this narrow window the reflection band position is essentially unchanged, indicating a locally flat region of the broader radius dependence shown in Figure 4 rather than a contradiction of it. Practically, this means that small radius errors of a few nanometers, of the

kind expected from electron beam lithography and dry etching, are unlikely by themselves to shift a finished device out of its intended color, even though the coarser sweep in Figure 4 shows that radius is the primary lever for moving between colors across the full palette.

4.2 Tolerance of height

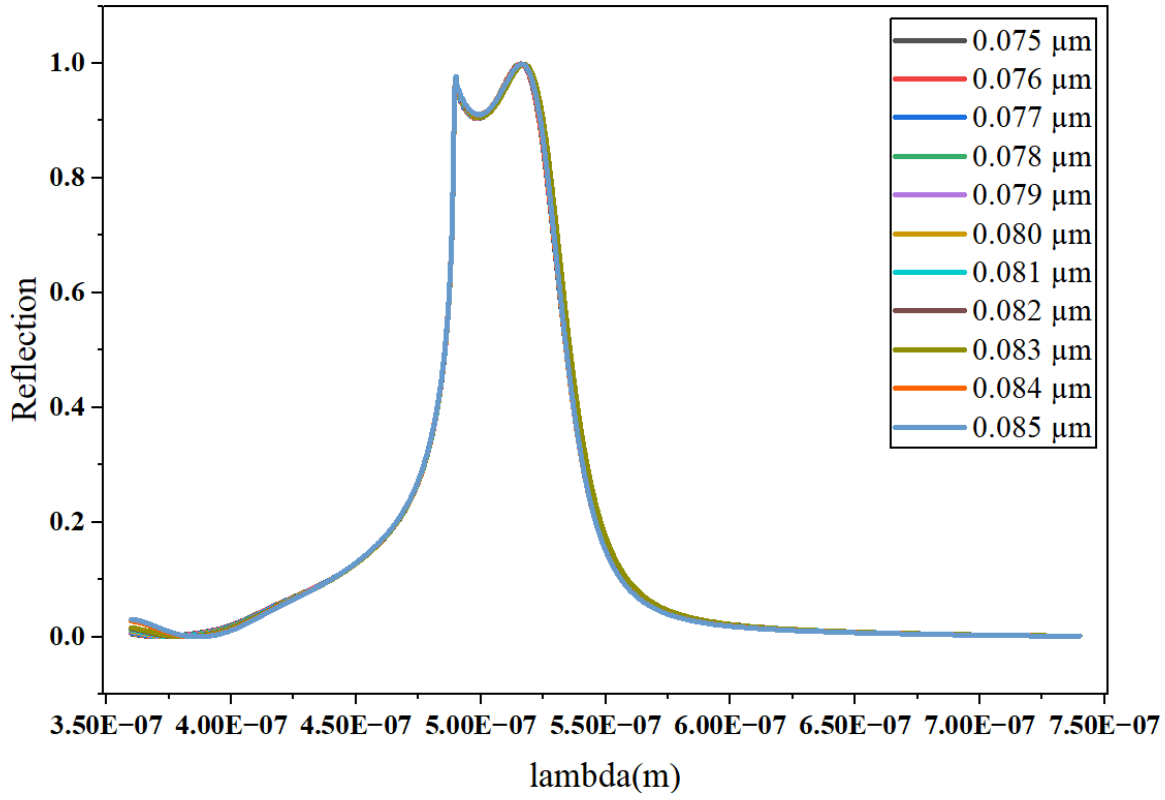


Figure 10. Fine height tolerance sweep. Reflectance spectra for the top $MAPbCl_3$ cladding thickness swept from 75 to 85 nm in 1 nm steps, with all other parameters held at their nominal design values.

Figure 10 sweeps the top MAPbCl3 cladding thickness from 75 to 85 nm in 1 nm steps, bracketing the nominal 80 nm design value. The eleven resulting spectra are essentially indistinguishable, both in peak position and in the shouldered lineshape near the resonance. This indicates that the design is highly insensitive to top layer height error at the scale expected from thin film deposition, a comparatively forgiving tolerance relative to the lateral dimensions.

4.3 Tolerance of period

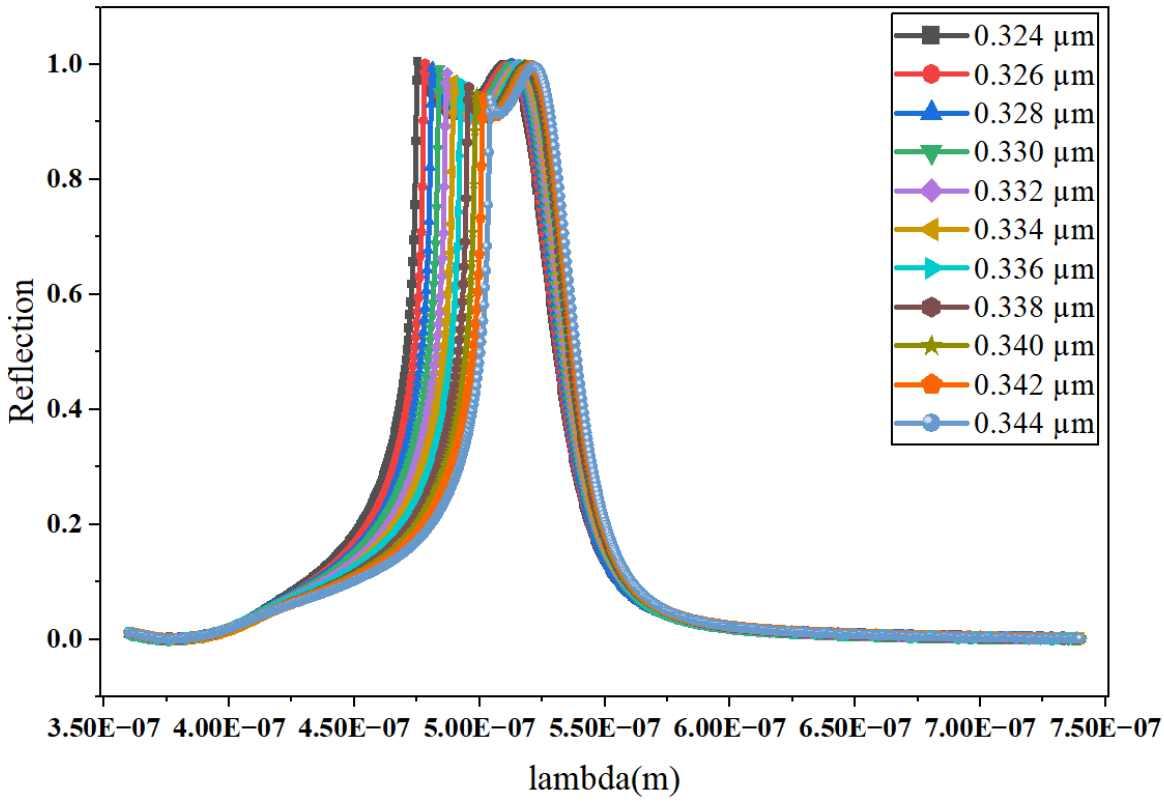


Figure 11. Fine period tolerance sweep. Reflectance spectra for the lattice period swept from 324 to 344 nm in 2 nm steps, with all other parameters held at their nominal design values.

Figure 11 sweeps the lattice period from 324 to 344 nm in 2 nm steps, bracketing the cyan design value. Unlike the height sweep, the eleven curves are clearly distinguishable. The short wavelength edge of the reflection band shifts by approximately 30 to 40 nm across the swept range, while the longer wavelength edge and the peak near 515 to 520 nm stay comparatively fixed. This pattern is consistent with the short wavelength edge being associated with the array period, most likely through a lattice coupled or diffraction related feature entering the spectral window as period increases, while the peak itself remains governed by the localized resonance of the individual meta-atom. Period control is therefore more consequential than height control for preserving the intended lineshape, and it should be prioritized accordingly during array patterning.

5. Conclusion

We have designed and numerically investigated an all-perovskite trilayer frustum metasurface consisting of $MAPbCl_3/CsPbI_3/MAPbCl_3$. The architecture transfers the gradient-index concept of multilayer dielectric structural-color resonators to a chemically unified halide-

perovskite platform. By retaining three fixed layer heights of 90/100/80 nm and varying the lateral radii and lattice period, seven representative colors were obtained with simulated reflectance peaks spanning 470–630 nm. The calculated linewidth decreases from approximately 63 to 19 nm across the palette, while near-field distributions of the red design are consistent with a magnetic-dipole-like Mie resonance concentrated primarily in the high-index $CsPbI_3$ region. The circular in-plane geometry provides polarization-insensitive behavior at normal incidence, and the angular simulations indicate that the resonance remains identifiable at substantially oblique incidence. CIE 1931 analysis places the calculated palette across a broad chromaticity region, with the shorter-wavelength designs extending beyond sRGB and the complete set lying within the reported Adobe RGB and Rec. 2020 reference triangles. These results establish a simulation-level proof of concept rather than an experimentally validated device. The principal practical challenge is stabilization of the black α-$CsPbI_3$ phase, together with accurate determination of the complex optical constants, film uniformity, interfacial quality, and perovskite-compatible nanofabrication. Future experimental work should therefore begin with optical-constant verification and phase-stability assessment before attempting nanoscale pattern transfer.

References

[1] H. Langhals, 'Color Chemistry. Synthesis, Properties and Applications of Organic Dyes and Pigments. 3rd revised edition. By Heinrich Zollinger.', *Angew. Chem. Int. Ed.*, vol. 43, no. 40, pp. 5291–5292, Oct. 2004, doi: 10.1002/anie.200385122.

[2] K. Kumar, R. Hegde, S. Koh, J. Wei, and J. Yang, 'Printing colour at the optical diffraction limit', *Nat. Nanotechnol.*, vol. 7, pp. 557–61, Aug. 2012, doi: 10.1038/nnano.2012.128.

[3] T. Xu, Y.-K. Wu, X. Luo, and L. J. Guo, 'Plasmonic nanoresonators for high-resolution colour filtering and spectral imaging', *Nat. Commun.*, vol. 1, no. 1, p. 59, Aug. 2010, doi: 10.1038/ncomms1058.

[4] J. Proust, F. Bedu, B. Gallas, I. Ozerov, and N. Bonod, 'All-Dielectric Colored Metasurfaces with Silicon Mie Resonators', *ACS Nano*, vol. 10, no. 8, pp. 7761–7767, Jul. 2016, doi: 10.1021/acsnano.6b03207.

[5] W. Yang *et al.*, 'All-dielectric metasurface for high-performance structural color', *Nat. Commun.*, vol. 11, no. 1, p. 1864, Apr. 2020, doi: 10.1038/s41467-020-15773-0.

[6] J. Walia, N. Dhindsa, M. Khorasaninejad, and S. S. Saini, ‘Color Generation and Refractive Index Sensing Using Diffraction from 2D Silicon Nanowire Arrays’, *Small*, vol. 10, no. 1, pp. 144–151, Jan. 2014, doi: 10.1002/smll.201300601.

[7] S. Sun *et al.*, ‘All-Dielectric Full-Color Printing with TiO2 Metasurfaces’, *ACS Nano*, vol. 11, no. 5, pp. 4445–4452, Mar. 2017, doi: 10.1021/acsnano.7b00415.

[8] M. R. Miah, Y. S. Aydın, and H. V. Demir, ‘Multi-Dielectric Metasurfaces for Ultrabright, Tunable Structural Color and Reconfigurable Optical Filtering with Extraordinarily Large Color Span’, *Adv. Opt. Mater.*, vol. 14, no. 23, p. e71173, Jun. 2026, doi: 10.1002/adom.71173.

[9] C. Cui *et al.*, ‘Light emission driven by magnetic and electric toroidal dipole resonances in a silicon metasurface’, *Nanoscale*, vol. 11, pp. 14446–14454, Jul. 2019, doi: 10.1039/C9NR03172C.

[10] T. Kaelberer, V. Fedotov, N. Papasimakis, D. P. Tsai, and N. Zheludev, ‘Toroidal Dipolar Response in a Metamaterial’, *Science*, vol. 330, pp. 1510–1512, Dec. 2010, doi: 10.1126/science.1197172.

[11] H. Dong, C. Ran, W. Gao, M. Li, Y. Xia, and W. Huang, ‘Metal Halide Perovskite for next-generation optoelectronics: progresses and prospects’, *eLight*, vol. 3, Jan. 2023, doi: 10.1186/s43593-022-00033-z.

[12] L. Protesescu *et al.*, ‘Nanocrystals of Cesium Lead Halide Perovskites (CsPbX3, X = Cl, Br, and I): Novel Optoelectronic Materials Showing Bright Emission with Wide Color Gamut’, *Nano Lett.*, vol. 15, no. 6, pp. 3692–3696, Jan. 2015, doi: 10.1021/nl5048779.

[13] A. Yan, Y. Guo, C. Liu, Z. Deng, Y. Guo, and X. Zhao, ‘Tuning the Optical Properties of CsPbBr3 Nanocrystals by Anion Exchange Reactions with CsX Aqueous Solution’, *Nanoscale Res. Lett.*, vol. 13, Dec. 2018, doi: 10.1186/s11671-018-2592-4.

[14] H. Chen, M. Li, B. Wang, S. Ming, and J. Su, ‘Structure, electronic and optical properties of CsPbX3 halide perovskite: A first-principles study’, *J. Alloys Compd.*, vol. 862, p. 158442, Dec. 2020, doi: 10.1016/j.jallcom.2020.158442.

[15] A. S. Berestennikov, P. M. Voroshilov, S. V. Makarov, and Y. S. Kivshar, ‘Active meta-optics and nanophotonics with halide perovskites’, *Appl. Phys. Rev.*, vol. 6, no. 3, p. 031307, Sep. 2019, doi: 10.1063/1.5107449.

[16] J. Tian *et al.*, ‘Phase-change perovskite metasurfaces for dynamic color tuning’, *Nanophotonics*, vol. 11, no. 17, pp. 3961–3968, Sep. 2022, doi: 10.1515/nanoph-2022-0143.

[17] R. Singh, R. Kumar, N. Jain, S. Dash, J. Singh, and A. Srivastava, ‘Investigation of optical and dielectric properties of CsPbI3 inorganic lead iodide perovskite thin film’, *J. Taiwan Inst. Chem. Eng.*, vol. 96, Nov. 2018, doi: 10.1016/j.jtice.2018.11.001.

[18] W. Zia *et al.*, ‘Single-crystalline MAPbCl3 thin-films for photo- and X-ray voltaics’, *EES Sol.*, vol. 1, pp. 810–818, Aug. 2025, doi: 10.1039/D5EL00087D.

[19] W. Zia *et al.*, ‘MAPbCl3 Light Absorber for Highest Voltage Perovskite Solar Cells’, *ACS Energy Lett.*, vol. 9, no. 3, pp. 1017–1024, Feb. 2024, doi: 10.1021/acsenergylett.3c02777.

[20] H.-P. Hsu, L.-C. Li, M. Shellaiah, and K. W. Sun, ‘Structural, Photophysical, and Electronic Properties of CH3NH3PbCl3 Single Crystals’, *Sci. Rep.*, vol. 9, Sep. 2019, doi: 10.1038/s41598-019-49926-z.

[21] S. Zou *et al.*, ‘High Photoactive Black Phase Stability of Cspbi3 Nanocrystals Under Damp-Heat Conditions of 85°C and 85% Relative Humidity’, *SSRN Electron. J.*, Jan. 2022, doi: 10.2139/ssrn.4263639.

[22] K. S. Yee, ‘Numerical solution of initial boundary value problems involving Maxwell’s equations in isotropic media’, IEEE Trans. Antennas Propag., vol. 14, no. 3, pp. 302–307, May 1966, doi: 10.1109/TAP.1966.1138693.

[23] A. Taflove and S. C. Hagness, Computational Electrodynamics: The Finite-Difference Time-Domain Method, 3rd ed. Norwood, MA: Artech House, 2005.

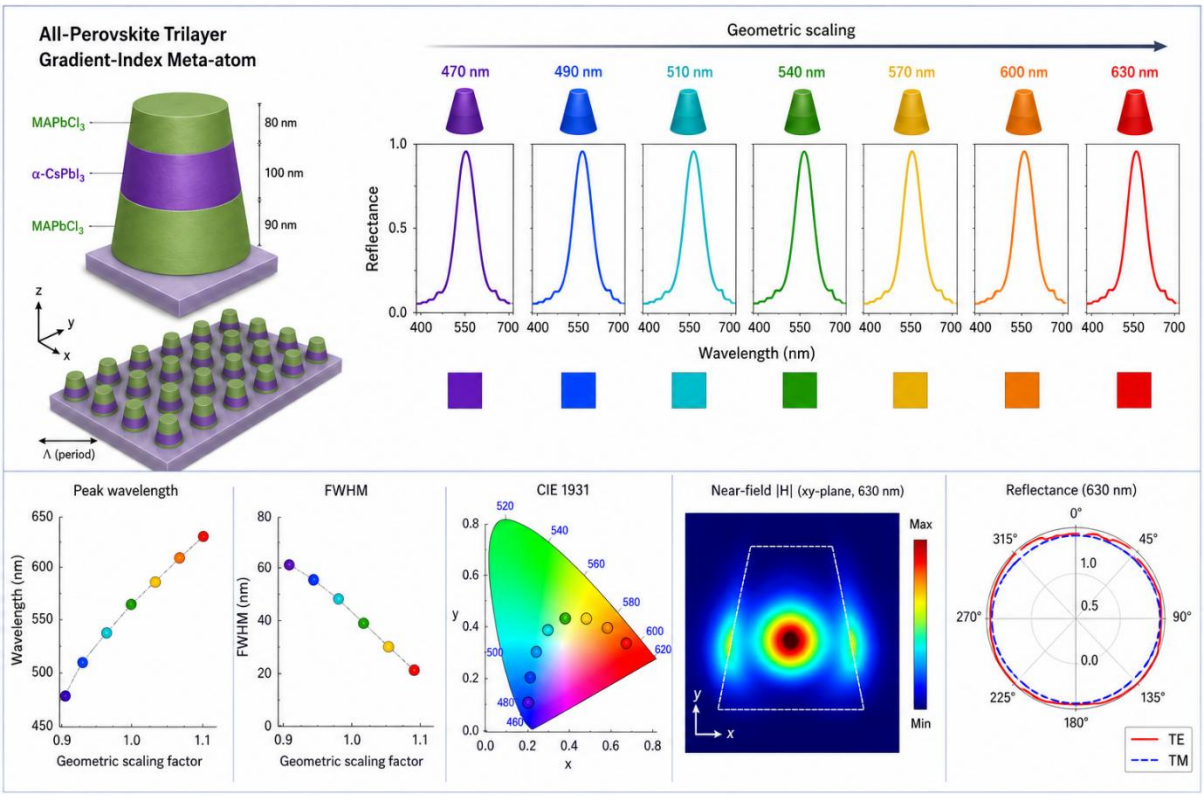
[24] T. Smith and J. Guild, ‘The C.I.E. colorimetric standards and their use’, Trans. Opt. Soc., vol. 33, no. 3, p. 73, Jan. 1931, doi: 10.1088/1475-4878/33/3/301.

[25] Z. Haddadin, S. Khan, and L. V. Poulikakos, ‘Cutting Corners to Suppress High-Order Modes in Mie Resonator Arrays’, ACS Photonics, vol. 11, no. 1, pp. 187–195, Jan. 2024, doi: 10.1021/acsphotonics.3c01270.

[26] Y. Gao et al., ‘Lead Halide Perovskite Nanostructures for Dynamic Color Display’, ACS Nano, vol. 12, no. 9, pp. 8847–8854, Sep. 2018, doi: 10.1021/acsnano.8b02425.

[27] B. Yang, W. Liu, Z. Li, H. Cheng, D.-Y. Choi, S. Chen, and J. Tian, ‘Ultrahighly Saturated Structural Colors Enhanced by Multipolar-Modulated Metasurfaces’, Nano Lett., vol. 19, no. 7, pp. 4221–4228, Jul. 2019, doi: 10.1021/acs.nanolett.8b04923.

TOC Only


All-Perovskite Trilayer
Gradient-Index Meta-atom
MAPbCl3
α-CsPbI3
MAPbCl3
80 nm
100 nm
90 nm
z
y
x
Λ (period)
Geometric scaling
470 nm
490 nm
510 nm
540 nm
570 nm
600 nm
630 nm
Reflectance
Wavelength (nm)
Peak wavelength
Wavelength (nm)
Geometric scaling factor
FWHM
FWHM (nm)
Geometric scaling factor
CIE 1931
Near-field |H| (xy-plane, 630 nm)
Max
Min
Reflectance (630 nm)
TE
TM